Supplementary Information

to

Pore Closure in Zeolitic Imidazolate Frameworks Under Mechanical Pressure

Sebastian Henke,[a]* Michael T. Wharmby,[b#] Gregor Kieslich,[c] Inke Hante,[d] Andreas Schneemann,[c%] Yue Wu,[e] Dominik Daisenberger[b] and Anthony K. Cheetham[e]

[a] *Anorganische Chemie, Fakultät für Chemie & Chemische Biology, Technische Universität Dortmund, Otto-Hahn-Straße 6, 44227 Dortmund, Germany.*
[b] *Diamond Light Source Ltd., Harwell Science & Innovation Campus, Didcot, Oxfordshire, OX11 0DE, UK.*
[c] *Lehrstuhl für Anorganische und Metallorganische Chemie, Technische Universität München, Lichtenbergstr. 4, 85748 Garching, Germany.*
[d] *Lehrstuhl für Anorganische Chemie II, Fakultät für Chemie & Biochemie, Ruhr-Universität Bochum, Universitätsstraße 150, 44801 Bochum, Germany.*
[e] *Department of Materials Science and Metallurgy, University of Cambridge, 27 Charles Babbage Road, Cambridge CB3 0FS, United Kingdom.*

[#] *Present address: Deutsches Elektronen-Synchrotron (DESY), Notkestr. 85, 22607 Hamburg, Germany.*
[%] *Present address: Sandia National Laboratories Livermore, CA 94551-0969, USA.*

Email: sebastian.henke@tu-dortmund.de

Contents

1. Synthesis and Activation

ZIF-4(Zn) (**1**) was prepared according to literature protocols[1, 2] and ZIF-4(Co) (**2**)[3] was prepared according to the following procedure:

$Co(NO_3)_2 \cdot 6H_2O$ (1.4 g, 4.8 mmol) and imidazole (Him; 0.9 g, 13 mmol) were dissolved in DMF (90 mL). The obtained solution was divided in 10 ~9 mL portions which were transferred into 12 mL borosilicate vials. These were sealed tightly and heated in a preheated oven to 130°C for 48 h. After cooling to room temperature the divided portions were recombined, filtered and washed with DMF. The product **2**⊃DMF was obtained as large purple single crystals.

The as-prepared DMF-containing materials **1**⊃DMF and **2**⊃DMF were washed thoroughly with fresh DMF (2x 50 mL) and CH_2Cl_2 (3x 50 mL) and subsequently dried at 130°C under dynamic vacuum (approx. 10^{-2} mbar) for 16 h.

Elemental analysis data:
Elemental analyses (C, H, N) were performed at Mikroanalytisches Laboratorium KOLBE (Mülheim an der Ruhr). The activated samples were transferred into small Schlenk tubes inside a glove box to prevent adsorption of water from the atmosphere.

1: calc. C 36.12%, N 28.08%, H 3.03%; found C 36.31%, N 28.25%, H 2.92%.
2: calc. C 37.33%, N 29.02%, H 3.13%; found C 37.22%, N 28.89%, H 3.01%.

The elemental analysis data suggest complete activation of the materials and the absence of any guest molecules.

2. Structural Analysis of the ZIF-4 Phases

The crystal structure of as-prepared **1**⊃DMF and **2**⊃DMF (both containing DMF in their pores) have been reported by Tian *et al* and Park *et al*.[3-5] Recently, some of us have shown that desolvated **1** undergoes an ***op*** to ***cp*** transition upon cooling to 80 K under vacuum.[2] In that work, we refined the room temperature ***op*** structure of **1** against synchrotron PXRD data. The reported structure of **1**⊃DMF from single crystal diffraction data was used as the starting model, with protons and DMF guest molecules omitted.[5] The low temperature ***cp*** phase of **1** was subsequently solved on the basis of synchrotron PXRD data and refined using the Rietveld method.[2]

The refined crystal structures of the ***op*** and ***cp*** phases of **1** (CCDC code 1047055 and 1047056) do not include hydrogen atoms.[2] Hydrogen atoms have been added to the im^- linkers of these structures at geometrical positions using the program OLEX2.[6] Subsequently the solvent accessible void space was calculated using these modified crystal structures (both containing H atoms at the im^- linker) also using OLEX2 (probe radius 1.2 Å, approx. grid spacing 0.2 Å). We calculated void spaces of 39% and 9% of the unit cell volumes for the ***op*** and ***cp*** phases, respectively. The voids present in **1**-***op*** are interconnected and, hence, accessible to gases and solvents (Fig. S1). The small elliptical voids present in **1**-***cp*** are isolated, so that solvents or gas molecules are unable to enter them (Fig. S2). Each of these isolated voids exhibits a volume of only 38.6 $Å^3$. This volume would be much too small for a DMF molecule (the volume of one DMF molecule at room temperature amounts to ~128 $Å^3$; calculated based on its density: 0.948 g/cm^3 at 20°C) and would just be large enough to host a single molecule of water (the volume of one water molecule is ~30 $Å^3$). Hence, we conclude that the ***op-cp*** phase transition of **1** is only possible if the pores of the material are empty. Only very small amounts of small molecules (i.e. water) could still be hosted in the contracted ***cp*** phase.

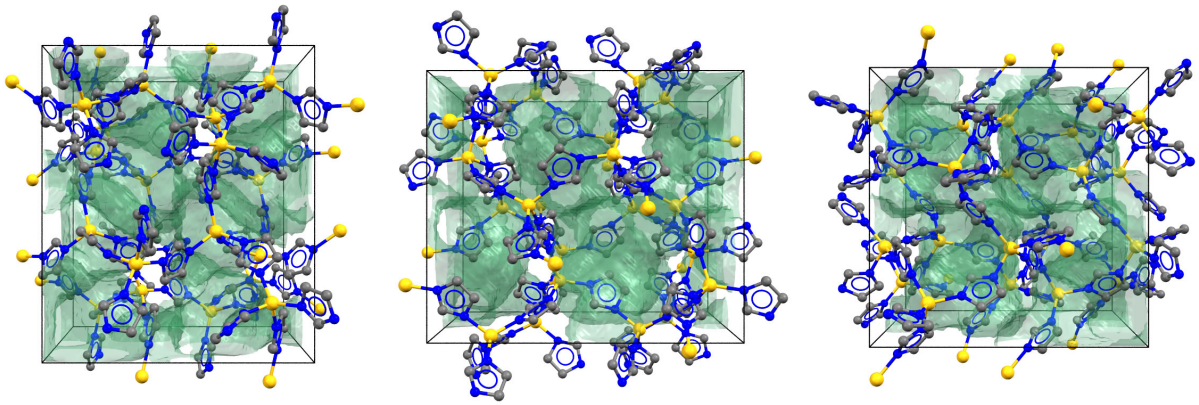

Fig. S1 The crystal structure of desolvated **1**-***op*** as determined from PXRD data recorded at 298 K in vacuum (taken from ref. 2). Views along the crystallographic *a* (left), *b* (middle) and *c* (right) axis are shown. C, N and Zn atoms are shown in grey, blue and yellow, respectively. The open void space is shown as green shades. The void space has been calculated by taking into account additional H atoms placed at geometrical positions at the im^- linkers.

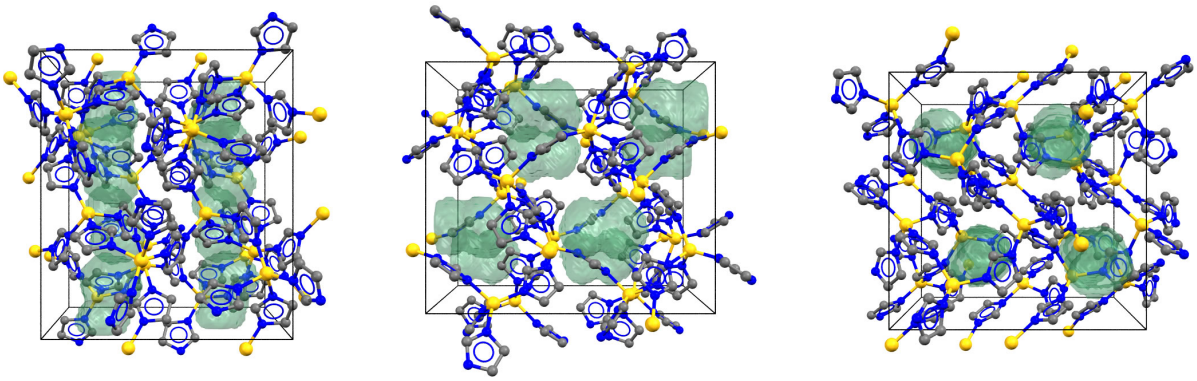

Fig. S2 The crystal structure of **1-*cp*** as determined from PXRD data recorded at 80 K in vacuum (taken from ref. 2). Views along the crystallographic *a* (left), *b* (middle) and *c* (right) axis are shown. C, N and Zn atoms are shown in grey, blue and yellow, respectively. The open void space is shown as green shades. The voids in the structure are inaccessible to gases and other guests, because they are isolated and not interconnected. The void space has been calculated by taking into account additional H atoms placed at geometrical positions at the im^- linkers.

The Zn atoms are tetrahedrally coordinated by N-donor atoms of im^-, in both phases, ***op*** and ***cp***. Two crystallographically independent Zn atoms are present in both structures. The distortion of a ZnN_4 tetrahedron is characterised by the deviation of its six im_x–Zn–im_y angles from the ideal tetrahedral angle (109.5°). The position of the im^- linkers is defined by the centroid of the imidazolate ring. In both phases the ZnN_4 tetrahedra are distorted from the ideal geometry, however, the distortion is much larger in the ***cp*** phase (see Fig. S3, Table S1). The distortion of the framework from its ideal geometry can also be evaluated by the Zn1–im–Zn2 angles of the four crystallographically independent im^- linkers. The ideal angle for such im^- linkers is ~144°.[4] Again, the Zn1–im–Zn2 angles of the ***cp*** phase deviate much more from the ideal angle (see Fig. S3, Table S2).

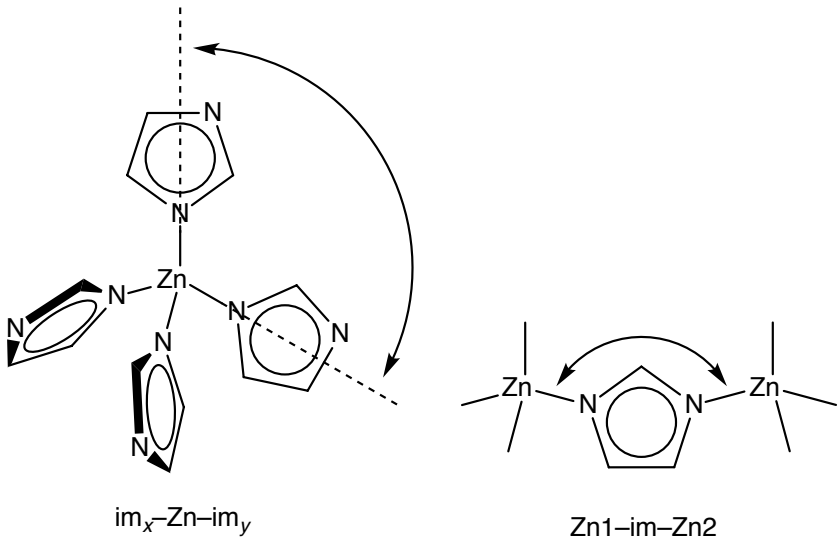

Fig. S3 Graphical representations of the representative crystallographic angles of the ZIF-4 building units compiled in Tables S1-S2.

Table S1 Comparison of the six im_x–Zn–im_y angles of the two crystallographically independent Zn atoms in the ***op*** and the ***cp*** phases of **1**. The data have been extracted from the crystallographic data given in ref. 2. The position of the im^- linkers is characterised by their plane centroids, which were calculated using OLEX2.[6] The mean angle and the mean deviation from the ideal tetrahedral angle (109.5°) are also given.

phase	central atom		angle 1	angle 2	angle 3	angle 4	angle 5	angle 6	mean
op	Zn1	absolute angle	110.5°	103.3°	118.2°	100.1°	110.5°	112.5°	109.2°
		deviation from ideal angle	1.0°	6.2°	8.7°	9.4°	1.0°	3.0°	4.9°
	Zn2	absolute angle	101.1°	111.5°	108.6°	117.5°	111.5°	106.8°	109.5°
		deviation from ideal angle	8.4°	2.0°	0.9°	8.0°	2.0°	2.7°	4.0°
cp	Zn1	absolute angle	102.2°	108.6°	137.1°	91.0°	96.1°	109.6°	107.4°
		deviation from ideal angle	7.3°	0.9°	27.6°	18.5°	13.4°	0.1°	11.3°
	Zn2	absolute angle	99.3°	100.7°	97.8°	125.0°	106.9°	120.2°	108.3°
		deviation from ideal angle	10.2°	8.8°	11.7°	15.5°	2.6°	10.7°	9.9°

Table S2 Comparison of the four Zn1–im–Zn2 angles of the four crystallographically independent im^- linkers in the ***op*** and the ***cp*** phases of **1**. The data have been extracted from the crystallographic data given in ref. 2. The mean angle and the mean deviation from the "ideal" im^- bonding angle (144°)[4] are also given.

phase	angle	im1	im2	im3	im4	mean
op	absolute angle	133.6°	139.3°	136.2°	142.0°	137.8°
	deviation from ideal angle	10.4°	4.7°	7.8°	2.0°	6.2°
cp	absolute angle	110.5°	141.0°	119.8°	128.0°	124.8°
	deviation from ideal angle	33.5°	3.0°	24.2°	16.0°	19.2°

3. Synchrotron High Pressure Powder X-ray Diffraction

High pressure PXRD measurements were performed at beamline I15 of Diamond Light Source (Oxon., UK) using a monochromatic X-ray beam ($\lambda = 0.41334$ Å; beamsize defined by 70 μm pinhole). Membrane Diamond Anvil Cells (mDACs) fitted with 900 μm culet diamonds and stainless steel gaskets (200 μm initial thickness; 500 μm diameter pressure chamber) were used as the pressure environment. A powdered sample of the ZIF was loaded into the chamber along with a ruby chip and an alkali halide internal pressure standard (NaCl for **1** and KBr for **2**). Fluorinert FC-70 (perfluorotripentylamine) was used as pressure transmitting fluid; the kinetic diameter of FC-70 exceeds the pore size of **1** and **2**, preventing penetration of the pressure transmitting fluid into the pores of the ZIFs. The cell was then sealed without membrane pressure and diffraction data collected using a MAR345 image plate detector for 60 seconds. Thanks to the small beamsize, it was possible to collect separate diffraction patterns of the sample and alkali halide. Membrane pressure was increased in steps of 1 bar up to the point at which the sample amorphised, with a measurement for the sample and the alkali halide collected at each pressure point. Diffraction data were integrated from 2D to 1D using the routines in the DAWN software suite.[7, 8]

The internal pressure of the mDAC chamber was determined from sequential Pawley refinements of the alkali halide pressure standard, performed using TOPAS-academic v6.[9] Pressures were calculated using the Vinet equations-of-state of Dorogokupets & Dewaele for NaCl[10] and Dewaele *et al.* for KBr[11].

Diffraction data for the samples were analysed by structure-less Pawley refinements performed with TOPAS academic v6.[9]

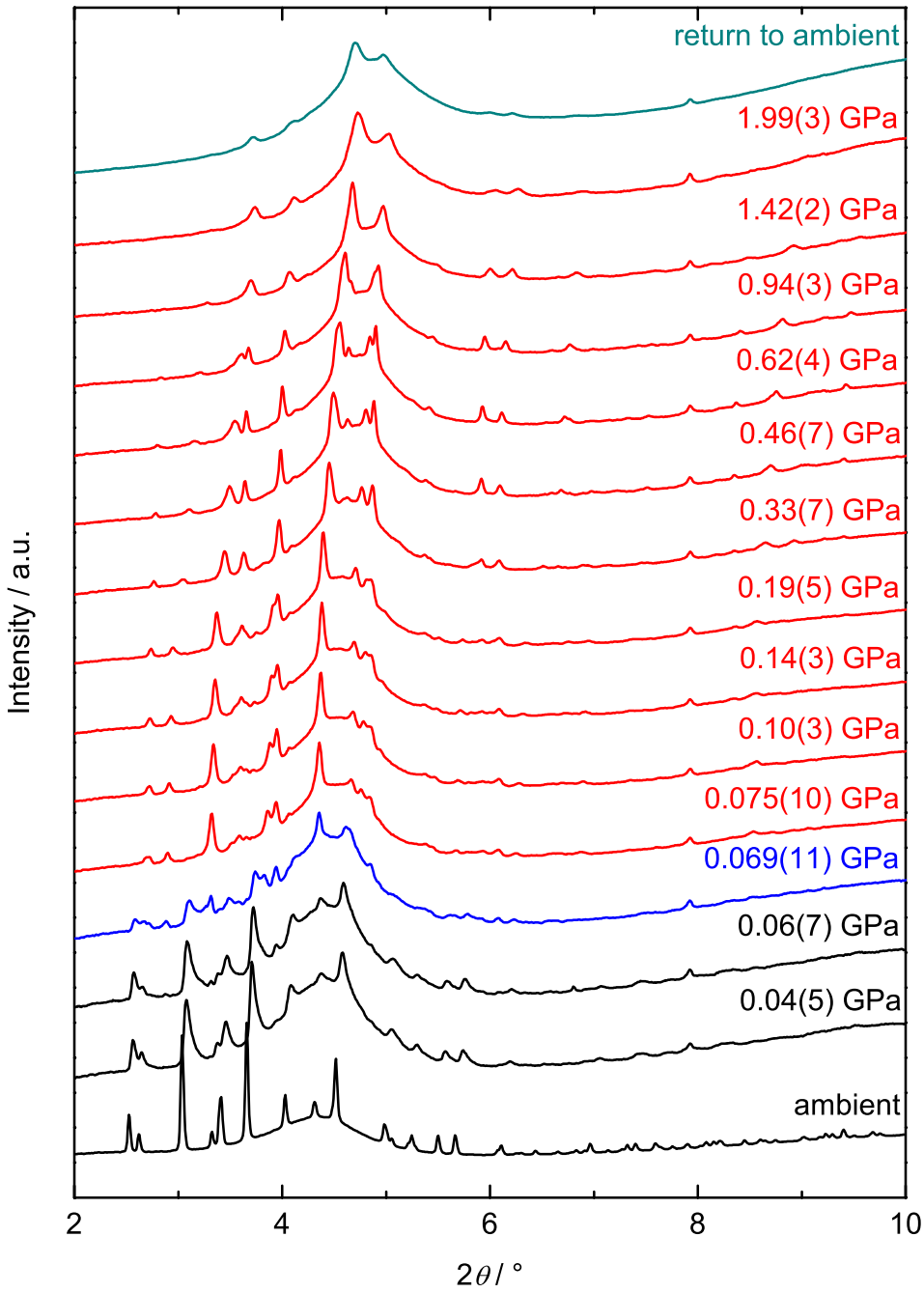

Fig. S4 Collection of normalised PXRD patterns (λ = 0.413339 Å) of **1** collected at variable mechanical pressure (mDAC with FC-70 as pressure transmitting fluid and NaCl as internal standard). For clarity the patterns have been offset along the vertical axis. Black patterns are assigned to the ***op*** phase, the blue pattern to a mixture of ***op*** and ***cp*** and the red patterns to the ***cp*** phase. The Bragg peaks of the ***cp*** phase get significantly broader and shift to higher Bragg angles with increasing mechanical pressure, which is in line with further compression of the framework. At pressures close to 1 GPa the reflections become very broad and peak intensity drops considerably. This may be assigned to significant amorphisation of the material[12], possibly as a consequence of leaving the hydrostatic limit of the pressure transmitting fluid FC-70.[13] Importantly, the largely amorphised sample does not recover its crystalline state after returning to ambient pressure (cyan pattern). This indicates irreversible framework contraction and amorphisation at high pressure.

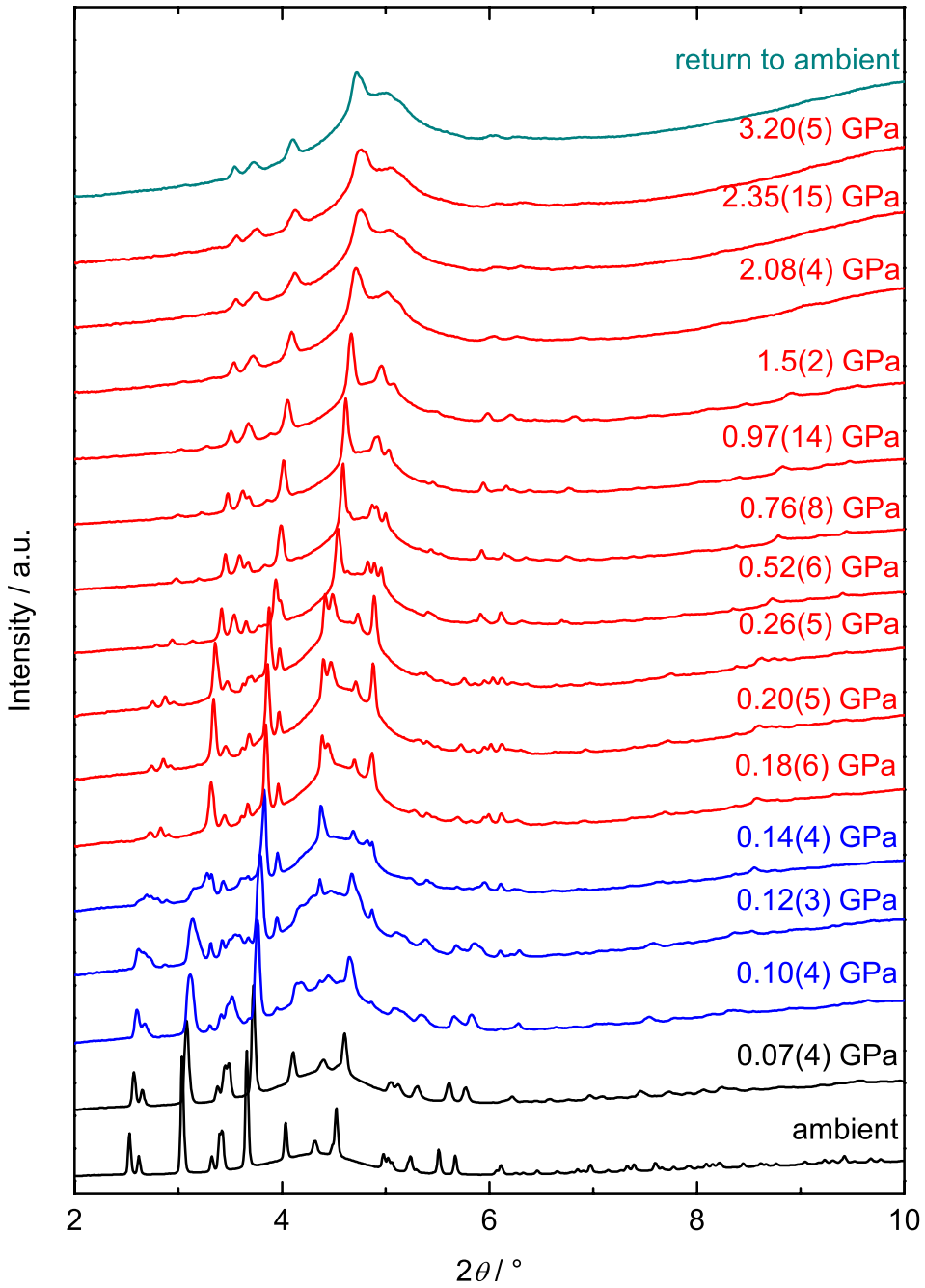

Fig. S5 Collection of normalised PXRD patterns (λ = 0.413339 Å) of **2** collected at variable mechanical pressure (mDAC with FC-70 as pressure transmitting fluid and KBr as internal standard). For clarity the patterns have been offset along the vertical axis. Black patterns are assigned to the ***op*** phase, blue patterns to mixtures of ***op*** and ***cp*** and red patterns to the ***cp*** phase. The Bragg peaks of the ***cp*** phase get significantly broader and shift to higher Bragg angles with increasing mechanical pressure, which is in line with further compression of the framework. At pressures above 1 GPa the reflections become very broad and peak intensity drops considerably. This may be assigned to significant amorphisation of the material[12], possibly as a consequence of leaving the hydrostatic limit of the pressure transmitting fluid FC-70.[13] Importantly, the largely amorphised sample does not recover its crystalline state after returning to ambient pressure (cyan pattern). This indicates irreversible framework contraction and amorphisation at high pressure.

Selected PXRD patterns of **1** and **2** have been fitted according to the Pawley method.[14] The patterns recorded at ambient pressure were fitted starting with unit cell parameters and space group symmetry from literature reference structure for the ***op*** phase of **1** (a = 15.50051(15) Å, b = 15.52013(14) Å, c = 18.05823(17) Å, space group *Pbca*).[2] The ambient pressure patterns of **1** and **2** could be fitted easily using these parameters and the obtained cell parameters are close to the reference values of compound **1** (see Fig. S6, S8 and Table S3). The patterns of the ***cp*** phase (at ~75 MPa for **1** and at ~180 MPa for **2**) were visually similar, but not identical to the diffraction pattern expected for the contracted low temperature ***cp*** phase of **1**.[2] Indeed, fitting the high pressure data to the unit cell of these low temperature phase (a = 14.26686(9) Å, b = 14.28427(8) Å, c = 16.41270(11) Å, space group *Pbca*)[2] was unsuccessful.

Visual inspection of the high pressure patterns indicated splitting of several Bragg peaks, which can only be explained by a reduction in unit cell symmetry. Consequently, we reduced the symmetry from orthorhombic to monoclinic, by adding a small shear (either α, β or $\gamma > 90°$; this angle was freely refined) and reducing the space group symmetry to one of the three possible monoclinic subgroups: $P112_1/a$ (with $\gamma > 90°$), $P12_1/c1$ (with $\beta > 90°$) and $P2_1/b11$ (with $\alpha > 90°$). Only in the subgroup $P12_1/c1$ could a satisfactory fit to the experimental data be obtained for the high pressure phases of both materials (see Fig. S7 and S9). The shear is small in both cases (β is close to 90°) and the lattice parameters a, b and c are similar to the lattice parameters of the orthorhombic ***cp*** reference structure, which has been determined at low temperature (see Table S3).[2] Hence, we conclude that the high pressure ***cp*** phases of **1** and **2** are topologically identical and structurally very similar to the previously reported ***cp*** phase of **1**.

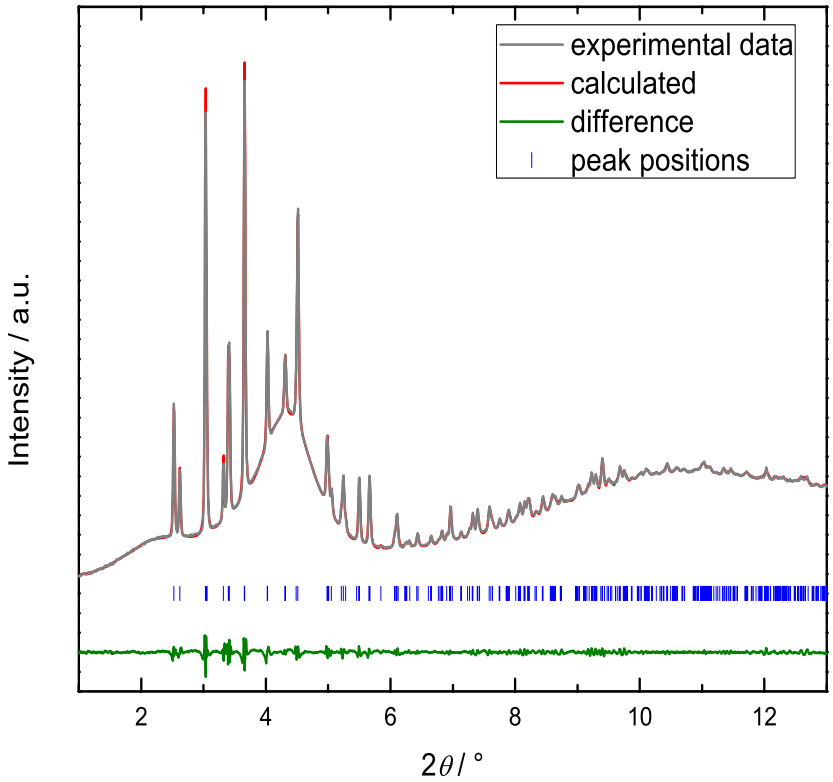

Fig. S6 Pawley fit to the diffraction pattern of **1** recorded at ambient pressure in a mDAC filled with FC-70 and NaCl (pressure standard). The very broad peak (centred at ~4.4°) underneath the Bragg peaks is ascribed to the diffuse scattering of the pressure transmitting fluid FC-70. Refinement parameters are listed in Table S3.

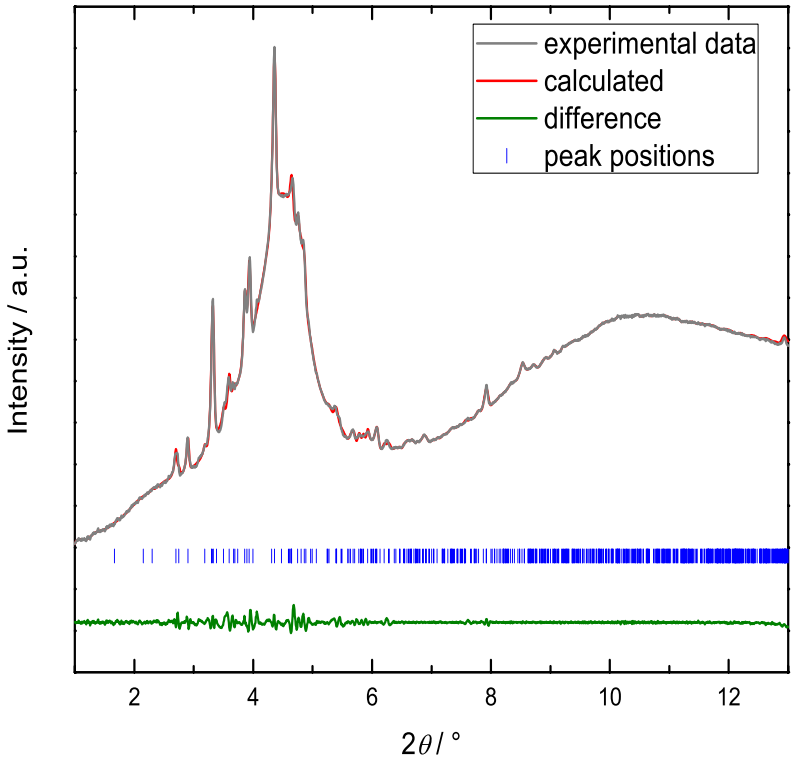

Fig. S7 Pawley fit to the diffraction pattern of **1** recorded at pressure of 75±10 MPa in a mDAC filled with FC-70 and NaCl (pressure standard). The very broad peak (centred at ~4.4°) underneath the Bragg peaks is ascribed to the diffuse scattering of the pressure transmitting fluid FC-70. Refinement parameters are listed in Table S3. A monoclinic unit cell which is related to the cell of the contracted orthorhombic low temperature phase of **1** (see ref. 2) has been used (see text for details).

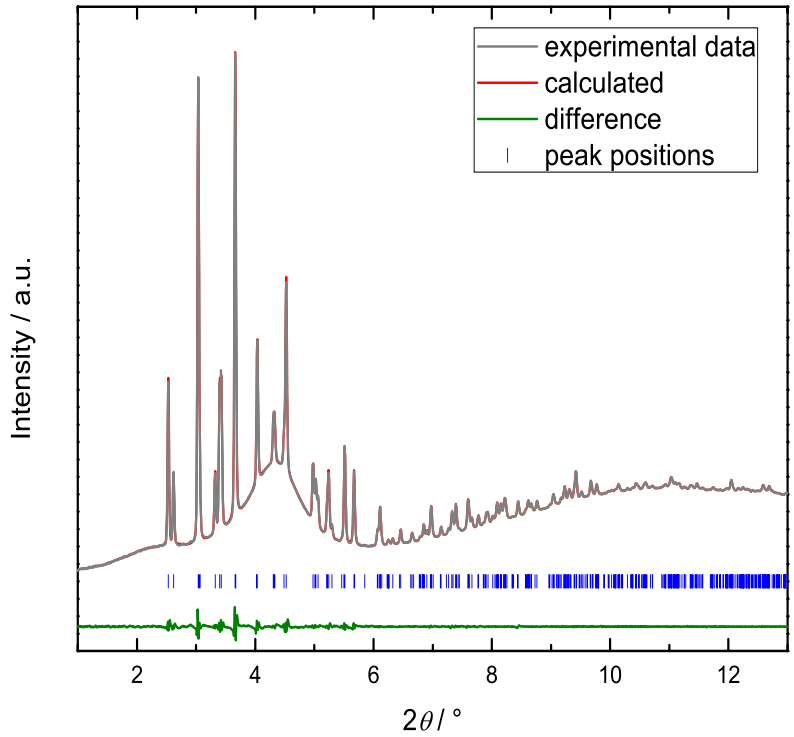

Fig. S8 Pawley fit to the diffraction pattern of **2** recorded at ambient pressure in a mDAC filled with FC-70 and KBr (pressure standard). The very broad peak (centred at ~4.4°) underneath the Bragg peaks is ascribed to the diffuse scattering of the pressure transmitting fluid FC-70. Refinement parameters are listed in Table S3.

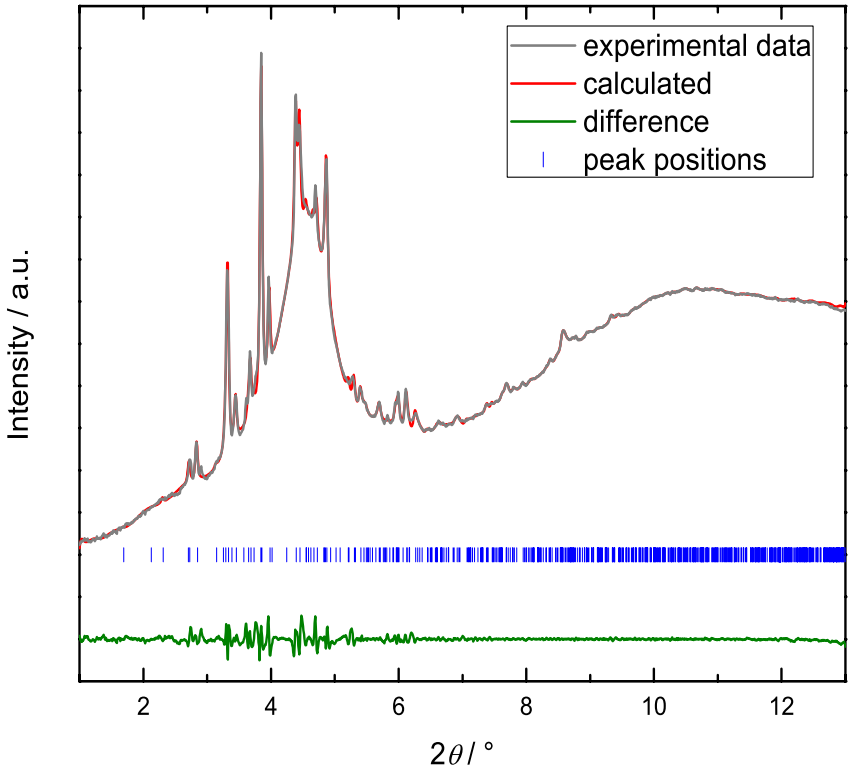

Fig. S9 Pawley fit to the diffraction pattern of **2** recorded at pressure of 180±60 MPa in a mDAC filled with FC-70 and KBr (pressure standard). The very broad peak (centered at ~4.4°) underneath the Bragg peaks is ascribed to the diffuse scattering of the pressure transmitting fluid FC-70. Refinement parameters are listed in Table S3. A monoclinic unit cell which is related to the cell of the contracted orthorhombic low temperature phase of ZIF-4(Zn) (see ref. 2) has been used (see text for details).

Table S3 Crystallographic data of the ambient pressure ***op*** and high pressure ***cp*** phases of **1** and **2** in comparison to literature reference data for the room temperature ***op*** and low temperature (80 K) ***cp*** phases of **1** (taken from ref. 2).

	1 at room temperature (***op*** phase)[a]	**1** at 80 K (***cp*** phase)[a]	Change in %	**1-*op***, at ambient pressure	**1-*cp***, at ~75 MPa	Change in %	**2-*op***, at ambient pressure	**2-*cp***, at ~180 MPa	Change in %
a / Å	15.50051(15)	14.26686(9)	–7.96	15.502(3)	14.235(12)	–8.17	15.440(2)	13.981(9)	–9.45
b / Å	15.52013(14)	14.28427(8)	–7.96	15.524(2)	14.874(18)	–4.19	15.5102(18)	15.045(13)	–3.00
c / Å	18.05823(17)	16.41270(11)	–9.11	18.079(3)	16.33(2)	–9.67	18.082(2)	16.636(15)	–8.00
α / °	90	90	–	90	90	–	90	90	–
β / °	90	90	–	90	91.55(3)	+1.72	90	90.761(11)	0.85
γ / °	90	90	–	90	90	–	90	90	–
V / Å^3	4344.27(7)	3344.77(4)	–23.01	4350.9(13)	3457(7)	–20.55	4330.1(9)	3499(5)	–19.19
space group	*Pbca*	*Pbca*	–	*Pbca*	$P2_1/c$	–	*Pbca*	$P2_1/c$	–
R_{wp}	–	–	–	0.695	0.382	–	0.512	0.616	–
R_{exp}	–	–	–	4.288	3.991	–	4.690	4.102	–
χ[b]	–	–	–	0.162	0.096	–	0.109	0.150	–

[a] see ref. 2; [b] $\chi = R_{wp}/R_{exp}$

4. Mercury Intrusion

Mercury intrusion experiments were performed on a Micromeritics Autopore IV 9500 porosimeter. Samples were thoroughly dried at 130°C under dynamic vacuum before the intrusion experiment. The sample tubes have been prepared insight an Ar-filled glove box to prevent any adsorption of moisture in the evacuated ZIFs. Two intrusion-extrusion cycles (compression-decompression) were performed on the dried samples (sample weight ~100 mg) in the range from ~10^{-3} to ~210 MPa. The volumes of intruded Hg have been corrected by a blank measurement using the same sample tube.

The effective pore diameter can be obtained from the mercury intrusion data by applying the Washburn equation, which assumes a cylindrical pore shape[15]:

$$p = -\frac{4\gamma\cos\theta}{d};$$

Where p is applied pressure, γ is the surface tension of Hg (0.485 N/m), θ is the contact angle between the solid and Hg (taken as 130°, in accordance with previous studies[16-18]), and d is the effective pore diameter.

A plot of the effective pore diameter vs. the differential intrusion volume for materials **1** and **2** is shown in Fig. S10 and S11. The step in the intrusion curves, that is ascribed to the ***op-cp*** phase transitions of these materials, would be ascribed to a pore diameter of about 40-50 nm for **1** and about 20 nm for **2**. Such pores are certainly not present in either material, so that these steps in the intrusion curves can only be ascribed to the ***op-cp*** phase transitions.

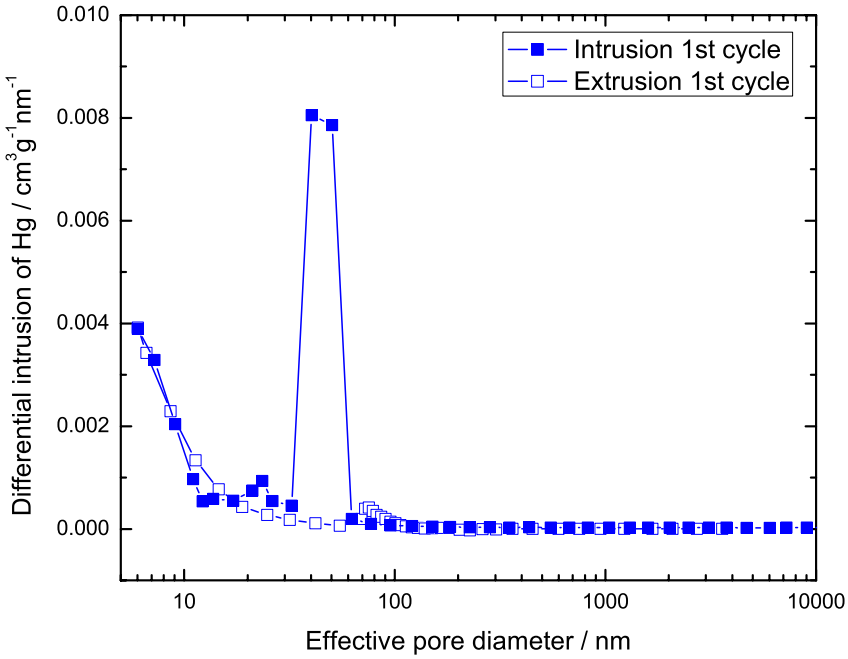

Fig. S10 Plot of the effective pore diameter vs. differential intrusion volume of Hg for **1**. The data have been calculated from the first intrusion-extrusion cycle using the Washburn equation. Lines are shown as a guide to the eye only. The step in the intrusion curve (see main text) occurs at a pressure of about 28 MPa, which relates to an effective pore diameter of about 40-50 nm. Since **1** does not feature pores in this range, the step in the intrusion curve can solely be ascribed to the ***op-cp*** phase transition. The transition results in an abrupt contraction of the material that is apparent as a sharp step in the intrusion curve.

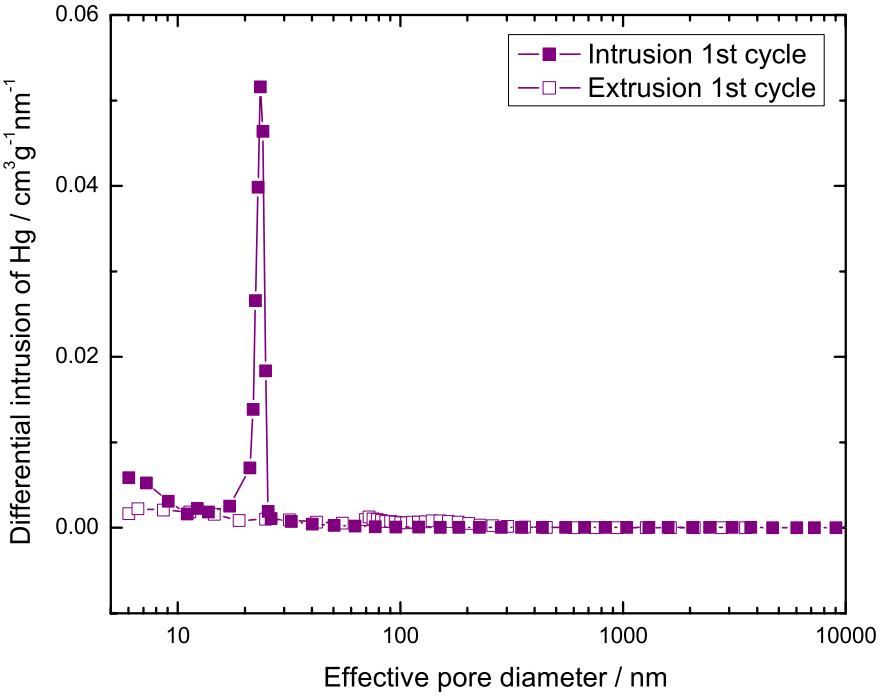

Fig. S11 Plot of the effective pore diameter vs. differential intrusion volume of Hg for **2**. The data have been calculated from the first intrusion-extrusion cycle using the Washburn equation. Lines are shown as a guide to the eye only. The step in the intrusion curve (see main text) occurs at a pressure of about 50 MPa, which relates to an effective pore diameter of about 20 nm. Since **2** does not feature pores in this range, the step in the intrusion curve can solely be ascribed to the ***op*-*cp*** phase transition. The transition results in an abrupt contraction of the material, which is apparent as a sharp step in the intrusion curve. The reverse ***cp*-*op*** transition does not generate a peak, because of its shallow profile in the extrusion curve.

The bulk modulus (K_i) for the ***op*** and ***cp*** phases of **1** and **2** can be estimated from the mercury intrusion curves.

$$K_i = -V\frac{\partial p}{\partial V};$$

Where V is volume and p pressure.

We define the slope of the intrusion curve (s_i) as follows:

$$s_i = \frac{d\left(\frac{V_{\text{intruded}}}{m_{\text{sample}}}\right)}{dp};$$

Where $V_{\text{intruded}}/m_{\text{sample}}$ is the volume of intruded Hg per mass of sample.

The slopes (s_i) of the linear regions after intrusion of Hg in the inter-particle voids but before the phase transition (7 – 25 MPa for **1** and 10 – 50 MPa for **2**) are used to estimate K_i for the ***op*** phases of these materials. The slopes (s_i) of the linear regions after the phase transition up to the highest pressure (40 – 210 MPa for **1** and 75 – 210 MPa for **2**) are used to estimate K_i for the respective ***cp*** phases. This is reasonable because the change in volume of intruded Hg ($\Delta V_{\text{intruded}}$) is equivalent to the change in unit cell volume $\Delta V_{\text{unit cell}}$. The compressibility of mercury is taken out of the equation by correcting the data by a blank measurement (see

above). The following equation applies:

$$\frac{\Delta V_{\text{intruded}}}{m_{\text{sample}}} = -\frac{\Delta V_{\text{unit cell}} \cdot N_A}{Z \cdot M_{\text{sample}}};$$

Where $\Delta V_{\text{intruded}}/m_{\text{sample}}$ is the change in volume of intruded Hg per mass of sample, N_A is Avogadro's constant, Z is the number of formula units per unit cell (16 for both phases of **1** and **2**), M_{sample} is the molar mass of the sample.

The bulk modulus (K_i) can been calculated according to the following equation:

$$K_i = \frac{V_{0,i} \cdot N_A}{Z \cdot s_i \cdot M};$$

Where $V_{0,I}$ is the crystallographic unit cell volume of the ***op*** and ***cp*** phases as determined by powder X-ray diffraction (see Table S4).

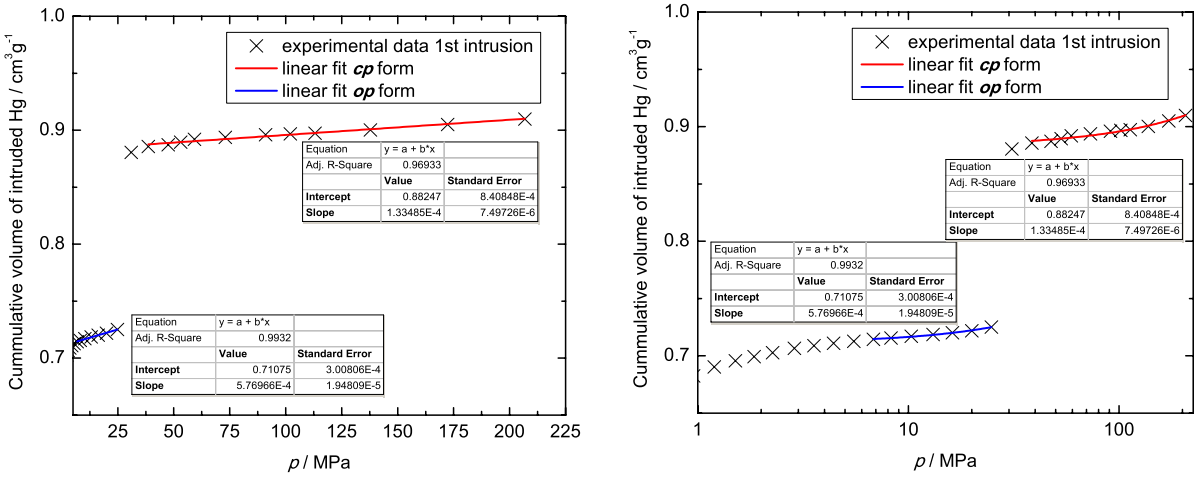

Fig. S12 Linear fits to the mercury intrusion data (1st cycle) recorded for **1**. The linear regions for the compression of the ***op*** form (7 – 25 MPa, blue line) and of the ***cp*** form (40 – 210 MPa, red line) have been fit individually. The fitting parameters are tabulated in the insets. The slope of these fits is used to calculate the bulk modulus of the two phases (see above). Left: Plot with a linear pressure axis. Right: Plot with a logarithmic pressure axis.

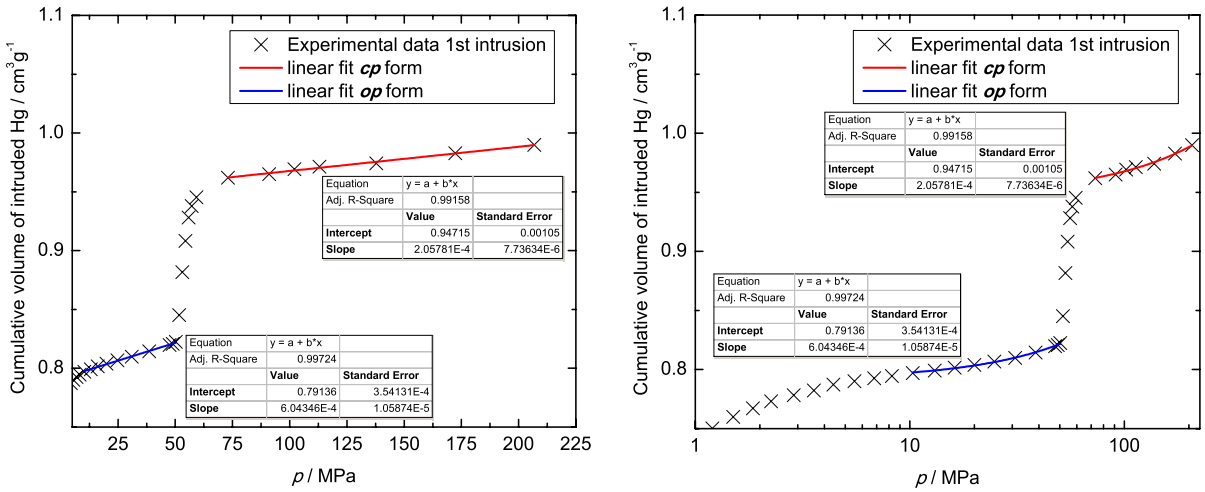

Fig. S13 Linear fits to the mercury intrusion data (1st cycle) recorded for **2**. The linear regions for the compression of the ***op*** form (10 – 50 MPa, blue line) and of the ***cp*** form (75 – 210 MPa, red line) have been fit individually. The fitting parameters are tabulated in the insets. The slope of these fits is used to calculate the bulk modulus of the two phases (see above). Left: Plot with a linear pressure axis. Right: Plot with a logarithmic pressure axis.

Table S4 Estimated bulk moduli of the ***op*** and ***cp*** phases of compounds **1** and **2**. The data have been calculated from the first intrusion cycle (see Fig. S12 and S13). We note, that the bulk moduli calculated from the second intrusion cycle of **2** are virtually identical to the values calculated from the first cycle.

compound	K_{op} / GPa	K_{cp} / GPa
1	1.42	4.88
2	1.40	3.31

The work done on the ZIFs during the ***op-cp*** phase transition ($W_{op\text{-}cp}$) can also be estimated from the mercury intrusion data:

$$W_{op\text{-}cp} = -p_{\text{trans}} \cdot \Delta V_{op\text{-}cp}$$

Where p_{trans} is the phase transition pressure and $\Delta V_{op\text{-}cp}$ is the volume change during the ***op-cp*** phase transition.

Table S5 Estimated work done on the ZIFs during the ***op-cp*** phase transition.

compound	p_{trans} / MPa	$\Delta V_{op\text{-}cp}$ / cm^3 g^{-1}	$W_{op\text{-}cp}$ / J g^{-1}
1	28	–0.16	4.4
2	50	–0.15	7.3

5. *Ex Situ* Compression Experiment

PXRD measurements for the *ex situ* compression experiment were performed in house on a Bruker D8 Advance diffractometer using Cu $K\alpha$ (λ = 1.5418 Å) radiation and a fitted with LynxEye position sensitive detector in Bragg-Brentano (θ-θ) geometry over a 2θ range of 5° - 50° at room temperature.

For comparison with the *in situ* studies, a compression experiment of **1** was performed using a conventional pellet press, as typically used for the preparation of KBr pellets for IR spectroscopy (pellet diameter = 13 mm). 80 mg of freshly evacuated and finely ground **1** were placed in a pellet press and compacted until a stable pressure of ~190 MPa was reached. The sample was left to rest at that pressure for 10 minutes, before the pressure was released. The pellet of compacted **1** was then finely ground again and a PXRD pattern was recorded (Figure S13, red pattern). Afterwards, the compacted compound was heated to 130°C for 8 h before another diffraction pattern was recorded (Fig. S14, orange pattern).

In comparison to the mercury intrusion and the high-pressure diffraction experiments, the pressure is not applied hydrostatically to the sample here; rather, it is applied uniaxially in the pellet press. Hence the obtained results are not directly comparable with the results obtained from the other two techniques. The significant peak broadening in the pattern of the compacted sample likely originates from increased shear stresses, which result from uniaxial and not hydrostatic compression. However, even in this simple experiment the phase transition of **1** from the ***op*** to the contracted ***cp*** phase can clearly be observed in the diffraction pattern of the sample after compression. The prominent Bragg peaks of the pelletised material can be ascribed to the ***cp*** form of **1**. However, peaks belonging to the ***op*** phase are still present, but with lower intensity, which we ascribe to the non-hydrostatic nature of the applied pressure. This may lead to a fraction of the material to remain in the ***op*** phase. Remarkably, after heating the pelletised material to 130°C for 8 h, the intensity of the Bragg peaks of the ***op*** phase increases again while the intensity of the peaks of the ***cp*** phase decreases significantly. Hence, the fraction of the ***op*** phase increases again at the expense of the ***cp*** phase. This suggests, that the ***cp*** phase of **1** can (at least partially) be transformed back to the ***op*** phase by heating.

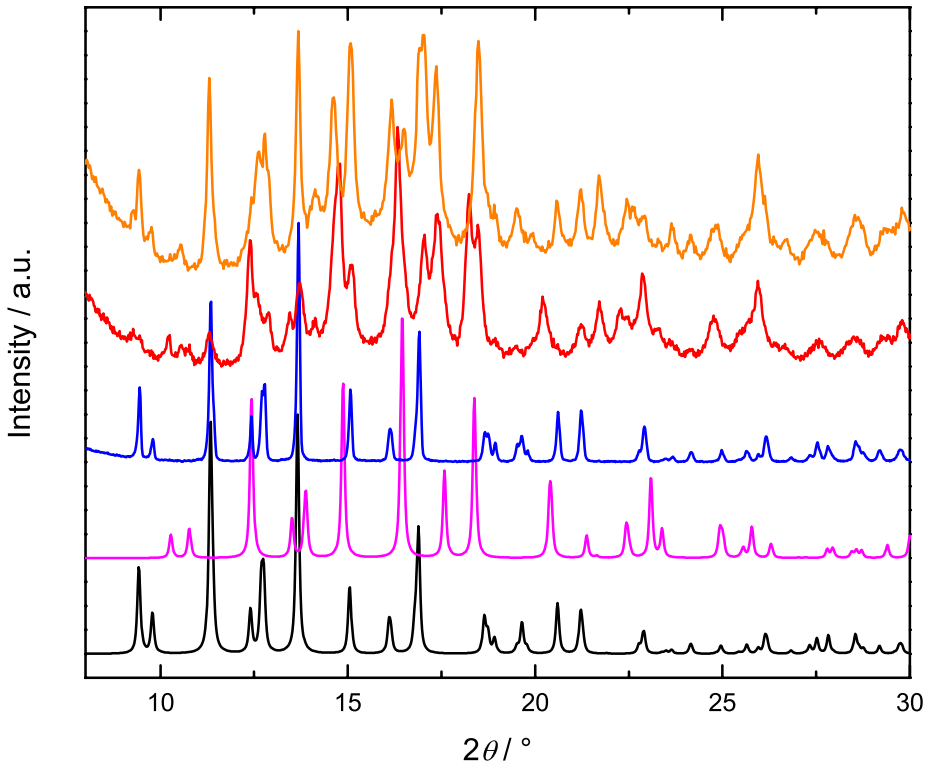

Fig. S14 Normalised PXRD patterns of freshly activated **1** (blue pattern); **1** pelletised in a conventional pellet press with an applied pressure of ~190 MPa (red pattern); and pelletised **1** after heating to 130°C for 8 h (orange pattern). For comparison, the calculated diffraction patterns of the room temperature ***op*** phase (black pattern) and the low temperature ***cp*** phase (magenta pattern) are shown. These patterns have been calculated from the crystal structures reported in ref. 2. For clarity the patterns have been offset along the vertical axis.

6. Thermogravimetric Analysis

Thermogravimetric analyses (TGA) were performed on a TA Instruments Q600 (sample weight approximately 5-10 mg) under nitrogen flow (flow rate 100 mL min^{-1}) in the temperature range from 25°C to 800°C with a heating rate of 10°C min^{-1}. For the measurement, samples were placed in alumina crucibles.

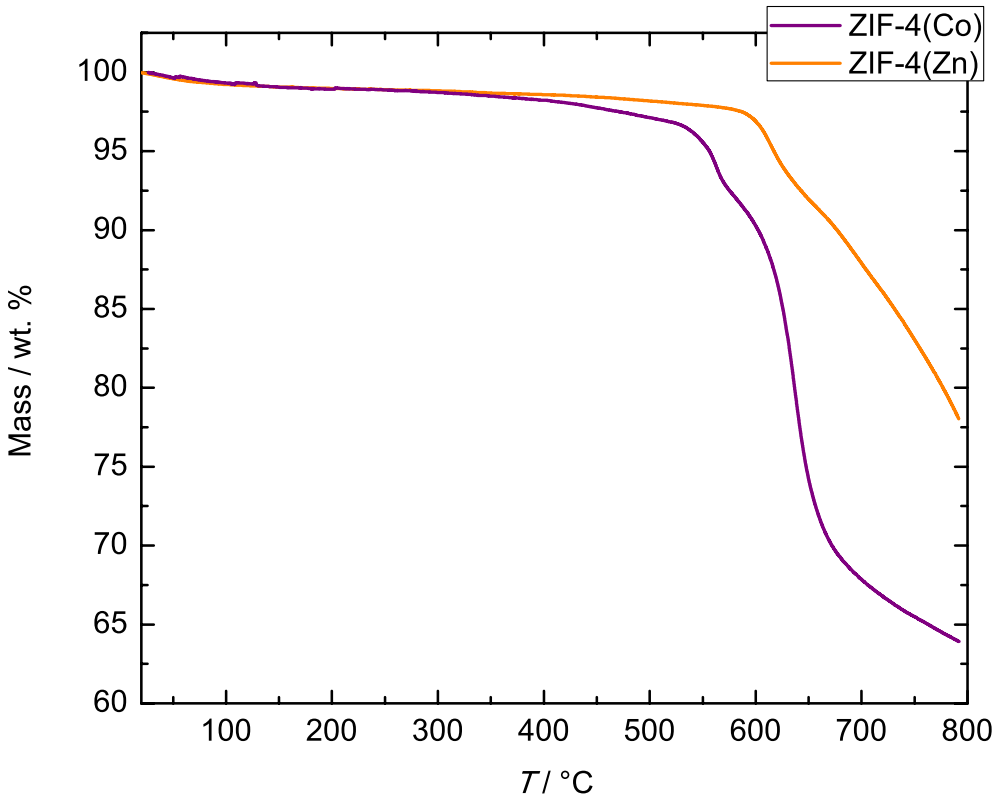

Fig. S15 TGA trace of the desolvated ZIF-4(Zn) (**1**) and ZIF-4(Co) (**2**) materials used in this study.

A weight loss of ~1% is detected in the range from 25°C to 200°C. We ascribe this to the evaporation of moisture from the sample, which was adsorbed during preparation of the sample for TGA under ambient atmosphere.

7. IR Spectroscopy

IR spectroscopy was carried out on a Bruker Tensor 27 FTIR spectrometer ($\tilde{\nu}$ = 520 cm^{-1} – 4000 cm^{-1}) in reflection mode using a diamond ATR (attenuated total reflectance) unit. The ZIF samples have been desolvated before the measurements (~10^{-2} mbar, 130°C). The reference spectrum of DMF was recorded by placing a droplet of DMF on the ATR crystal.

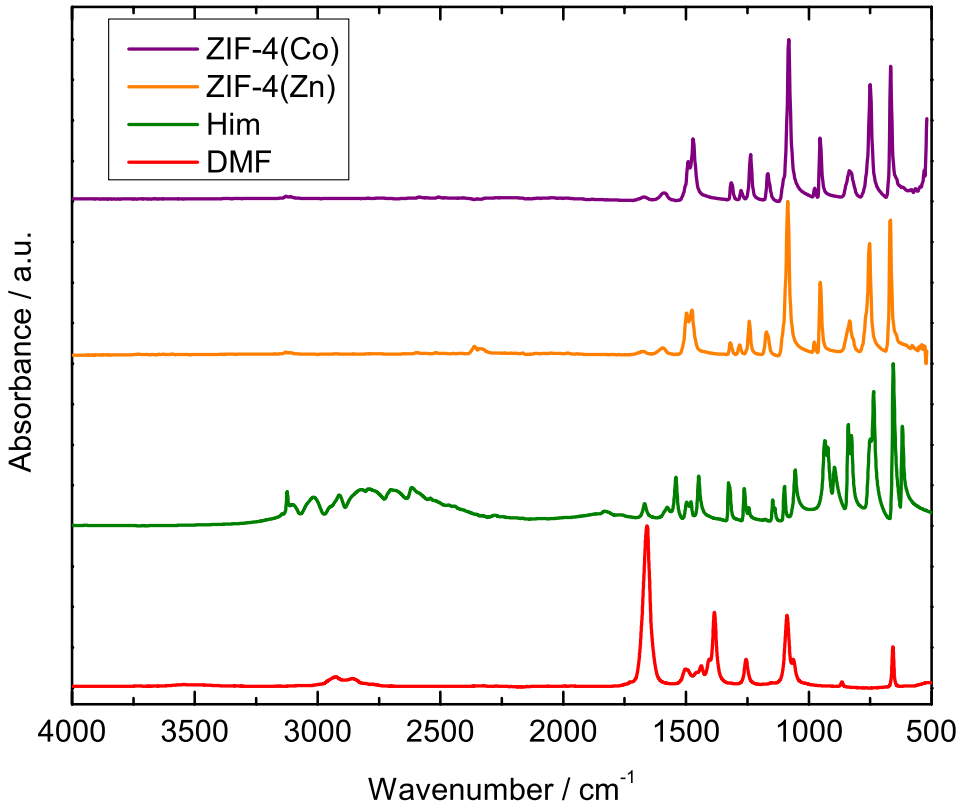

Fig. S16 ATR-FTIR spectra of the desolvated ZIF-4 materials used in this study in comparison to the spectra of solid Him (imidazole) and liquid DMF. The absence of the characteristic vibrational bands of DMF in the spectra of the ZIF-4 materials shows the absence of DMF in the ZIF materials. For clarity the spectra have been offset along the vertical axis.

The prominent peak for the carbonyl stretch of DMF is centred at 1659 cm^{-1}. The spectra of ZIF-4(Zn) (**1**) and ZIF-4(Co) (**2**) feature a weak peak at a similar frequency (centred at 1672 cm^{-1}). Furthermore the spectrum of pure Him also features a resonance peak at ~1670 cm^{-1}. The IR spectroscopy data, together with the elemental analysis and ^{1}H NMR spectroscopy data, strongly suggest that the peak at 1672 cm^{-1} is a feature of the framework vibrations and does not correspond to residual DMF in the ZIFs. The spectrum of DMF additionally features a prominent peak at 1384 cm^{-1}, which has about half the intensity of the strong peak for the carbonyl stretching vibration. This peak, however, is absent in the spectra of **1** and **2**, which again underlines the absence of DMF in the activated ZIFs.

8. ^{1}H NMR Spectroscopy

^{1}H NMR spectra of digested ZIF samples have been recorded on a 500 MHz NMR spectrometer DD2-500 (Agilent Technologies) equipped with a 5 mm triple resonance H(F,X) probe using DMSO-d_6 (0.5 mL) and DCl/D_2O (35 wt%, < 0.1 mL) as solvents. The data have been processes in SpinWorks 4.[19] The spectra have been referenced on the residual proton signal of DMSO and chemical shifts are given relative to TMS (tetramethylsilane). The spectra confirm the absence of DMF and CH_2Cl_2 in the activated materials.

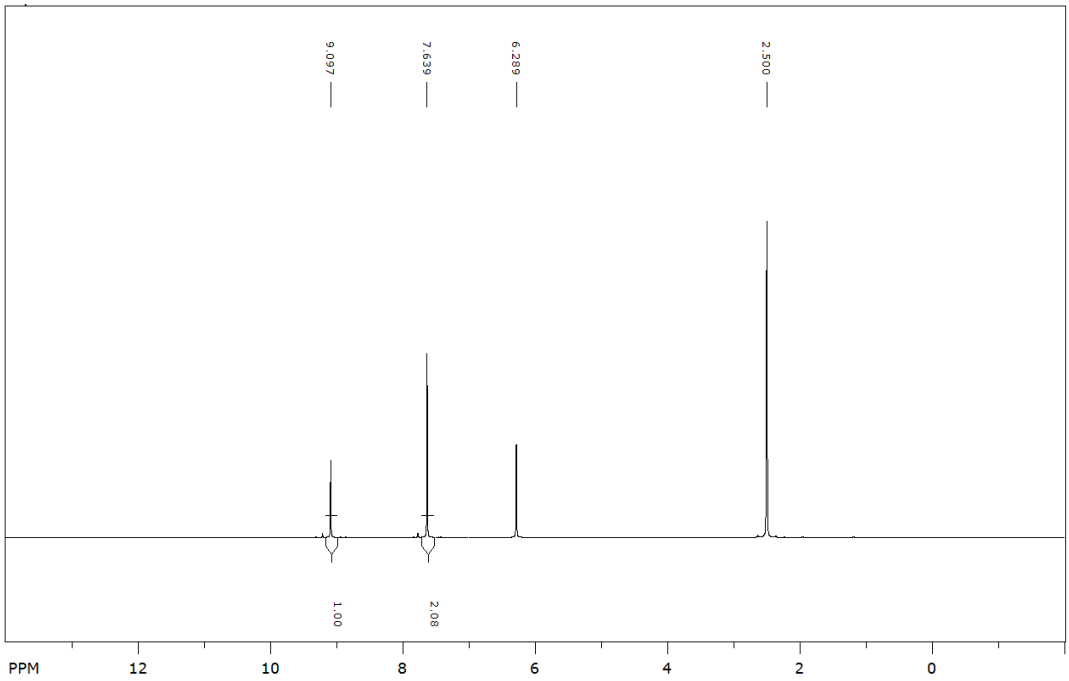

Fig. S17 ^{1}H NMR spectrum of a digested sample of **1**. Signals at 9.097 ppm and 7.639 ppm correspond to imidazolium. The signal at 6.29 ppm corresponds to HCl/H_2O and the signal at 2.50 ppm corresponds to DMSO.

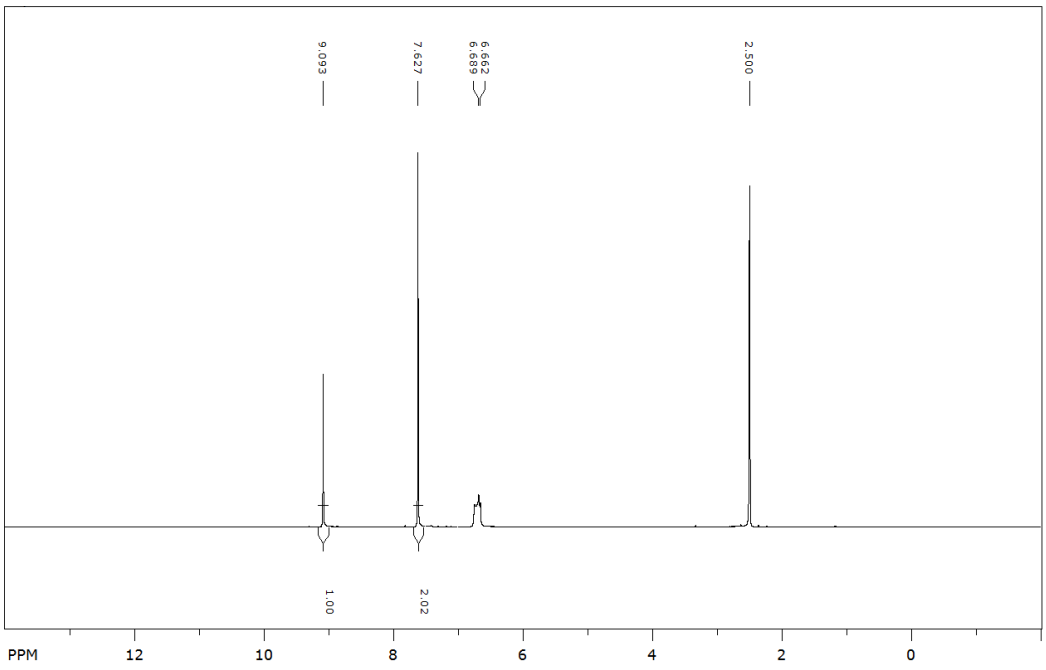

Fig. S18 ^{1}H NMR spectrum of a digested sample of **2**. Signals at 9.093 and 7.627 correspond to imidazolium. The signals at 6.6 ppm corresponds to HCl/H_2O and the signal at 2.50 ppm corresponds to DMSO.

References

1. M. R. Ryder, B. Civalleri, T. D. Bennett, S. Henke, S. Rudic, G. Cinque, F. Fernandez-Alonso and J. C. Tan, *Phys. Rev. Lett.*, 2014, **113**, 215502.
2. M. T. Wharmby, S. Henke, T. D. Bennett, S. R. Bajpe, I. Schwedler, S. P. Thompson, F. Gozzo, P. Simoncic, C. Mellot-Draznieks, H. Tao, Y. Yue and A. K. Cheetham, *Angew. Chem. Int. Ed.*, 2015, **54**, 6447-6451.
3. Y.-Q. Tian, Z.-X. Chen, L.-H. Weng, H.-B. Guo, S. Gao and D. Y. Zhao, *Inorg. Chem.*, 2004, **43**, 4631-4635.
4. Y. Q. Tian, Y. M. Zhao, Z. X. Chen, G. N. Zhang, L. H. Weng and D. Y. Zhao, *Chem. Eur. J.*, 2007, **13**, 4146-4154.
5. K. S. Park, Z. Ni, A. P. Cote, J. Y. Choi, R. Huang, F. J. Uribe-Romo, H. K. Chae, M. O'Keeffe and O. M. Yaghi, *Proc. Natl. Acad. Sci.*, 2006, **103**, 10186-10191.
6. O. V. Dolomanov, L. J. Bourhis, R. J. Gildea, J. A. K. Howard and H. Puschmann, *J. Appl. Cryst.*, 2009, **42**, 339-341.
7. J. Filik, A. W. Ashton, P. C. Y. Chang, P. A. Chater, S. J. Day, M. Drakopoulos, M. W. Gerring, M. L. Hart, O. V. Magdysyuk, S. Michalik, A. Smith, C. C. Tang, N. J. Terrill, M. T. Wharmby and H. Wilhelm, *J. Appl. Cryst.*, 2017, **50**, 959-966.
8. M. Basham, J. Filik, M. T. Wharmby, P. C. Chang, B. El Kassaby, M. Gerring, J. Aishima, K. Levik, B. C. Pulford, I. Sikharulidze, D. Sneddon, M. Webber, S. S. Dhesi, F. Maccherozzi, O. Svensson, S. Brockhauser, G. Naray and A. W. Ashton, *J. Synchrotron. Radiat.*, 2015, **22**, 853-858.
9. A. Coelho, *TOPAS-Academic v6*, (2016) Coelho Software, Brisbane.
10. P. I. Dorogokupets and A. Dewaele, *High Pressure Res.*, 2007, **27**, 431-446.
11. A. Dewaele, A. B. Belonoshko, G. Garbarino, F. Occelli, P. Bouvier, M. Hanfland and M. Mezouar, *Phys. Rev. B*, 2012, **85**, 214105.
12. T. D. Bennett, P. Simoncic, S. A. Moggach, F. Gozzo, P. Macchi, D. A. Keen, J. C. Tan and A. K. Cheetham, *Chem. Commun.*, 2011, **47**, 7983.
13. T. Varga, A. P. Wilkinson and R. J. Angel, *Rev. Sci. Instrum.*, 2003, **74**, 4564.
14. G. S. Pawley, *J. Appl. Cryst.*, 1981, **14**, 357-361.
15. H. Giesche, *Part. Part. Syst. Charact.*, 2006, **23**, 9-19.
16. P. G. Yot, Z. Boudene, J. Macia, D. Granier, L. Vanduyfhuys, T. Verstraelen, V. Van Speybroeck, T. Devic, C. Serre, G. Ferey, N. Stock and G. Maurin, *Chem. Commun.*, 2014, **50**, 9462-9464.
17. P. G. Yot, Q. Ma, J. Haines, Q. Yang, A. Ghoufi, T. Devic, C. Serre, V. Dmitriev, G. Férey, C. Zhong and G. Maurin, *Chem. Sci.*, 2012, **3**, 1100.
18. P. G. Yot, L. Vanduyfhuys, E. Alvarez, J. Rodriguez, J.-P. Itié, P. Fabry, N. Guillou, T. Devic, I. Beurroies, P. L. Llewellyn, V. Van Speybroeck, C. Serre and G. Maurin, *Chem. Sci.*, 2016, **7**, 446-450.
19. SpinWorks 4.2.0, Copyright © 2015, Kirk Marat, University of Manitoba.